Plasmon-Induced Hot Carriers from Interband and Intraband Transitions in Large Noble Metal Nanoparticles

Hanwen Jin,[1] Juhan Matthias Kahk,[2] Dimitrios A. Papaconstantopoulos,[3] Aires Ferreira,[4] and Johannes Lischner[5,*]

[1] *Department of Materials, Imperial College London, South Kensington Campus, London SW7 2AZ, United Kingdom*

[2] *Institute of Physics, University of Tartu, W. Ostwaldi 1, Tartu 50411, Estonia*

[3] *Department of Computational and Data Sciences George Mason University, Fairfax, VA 22030, USA*

[4] *Department of Physics and York Centre for Quantum Technologies, University of York, York YO105DD, United Kingdom*

[5] *Department of Materials and the Thomas Young Centre for Theory and Simulation of Materials, Imperial College London, South Kensington Campus, London SW7 2AZ, United Kingdom*

(Received 17 February 2022; revised 22 March 2022; accepted 13 April 2022; published 26 May 2022)

Hot electrons generated from the decay of localized surface plasmons in metallic nanostructures have the potential to transform photocatalysis, photodetection, and other optoelectronic applications. However, the understanding of hot-carrier generation in realistic nanostructures, in particular the relative importance of interband and intraband transitions, remains incomplete. Here we report theoretical predictions of hot-carrier generation rates in spherical nanoparticles of the noble metals silver, gold, and copper with diameters up to 30 nm consisting of more than one million atoms obtained from an atomistic linear-scaling approach. As the nanoparticle size increases, the relative importance of interband transitions from *d* bands to *sp* bands relative to surface-enabled *sp*-band to *sp*-band transitions increases. We find that the hot-hole generation rate is characterized by a peak at the onset of the *d* bands, while the position of the corresponding peak in the hot-electron distribution can be controlled through the illumination frequency. In contrast, intraband transitions give rise to hot electrons, but relatively cold holes. Importantly, increasing the dielectric constant of the environment removes hot carriers generated from interband transitions, while increasing the number of hot carriers from intraband transitions. The insights resulting from our work enable the design of nanoparticles for specific hot-carrier applications through their material composition, size, and dielectric environment.

DOI: 10.1103/PRXEnergy.1.013006

I. INTRODUCTION

Metallic nanoparticles are highly efficient light absorbers when the light frequency matches the frequency of the localized surface plasmon (LSP) [1,2]. The LSP is a collective oscillation of the conduction electrons and gives rise to a large time-dependent dipole moment that couples strongly to the electric field of the light wave [3]. Importantly, the LSP is a strongly damped oscillation that decays on femtosecond time scales [4,5]. Several decay channels are possible: a radiative decay resulting in the emission of light, a decay into one or more electron-hole pairs, or decay mechanisms involving phonons [6]. The decay into one electron-hole pair is known as Landau damping and is considered to be the most relevant for the generation of energetic or "hot" carriers at the surface of the nanoparticle [7,8]. Such hot carriers can be harnessed to drive chemical reactions [9–13] or for photodetection [14–20], for example.

Despite the promise of hot-carrier devices for novel energy conversion and optoelectronic devices, many fundamental questions about the behavior of hot carriers remain unsolved. For example, the question whether plasmonic photocatalysis is primarily facilitated by hot-carrier-induced heating of the nanoparticle or hot-carrier

*j.lischner@imperial.ac.uk

transfer to the reactant has been the subject of much debate [21–25]. Addressing these questions is crucial for the development and optimization of hot-carrier devices. To understand and identify the key driving force of plasmonic photocatalysis, a detailed microscopic understanding of hot-carrier processes in realistic nanostructures is required. This is very challenging to achieve, however, because quantum-mechanical first-principles approaches—while being highly accurate—can currently only be applied to periodic systems [4,26–29] or small nanoparticles [30,31]. For example, Rossi and coworkers used *ab initio* time-dependent density functional theory to study hot-carrier generation in silver nanoparticles consisting of up to 561 atoms [31]. However, the radius of such a nanoparticle is only a few nanometers, much smaller than typical nanoparticles that are used in devices. To model larger nanoparticles, simplified electronic structure methods, such as the jellium [32,33] or spherical-well approaches [33–35], have been widely adopted. However, these methods only capture intraband transitions and lack a description of *d* bands. As a consequence, they cannot describe the evolution of interband and intraband contributions to hot-carrier generation as a function of nanoparticle size, nor do they shed light on the role played by *d* electrons in photocatalysis [36,37].

In this paper, we use an atomistic electronic structure techniques based on an accurate tight-binding Hamiltonian that includes *d* states and reproduces the band structure of *ab initio* calculations [38–42] to study hot-carrier generation rates in large nanoparticles of silver, gold, and copper with diameters up to 30 nm as such nanoparticles are widely used in experimental studies and hot-carrier devices. We find that hot-carrier generation rates in small nanoparticles with diameters of a few nanometers exhibit a moleculelike behavior with discrete peaks that evolve into a continuous distribution for larger nanoparticles. The hot-hole generation rates are characterized by a large peak at the onset of the *d* bands stemming from interband *d*-to-*sp* band transitions [43]. The corresponding peak in the hot-electron generation rate is closer to the Fermi level, but its position can be controlled through the light frequency. Moreover, intraband transitions are shown to yield a second peak in the hot-hole generation rate that lies close to the Fermi level and a corresponding peak in the hot-electron rate at high energies. As the nanoparticle size increases, the interband transitions dominate increasingly over surface-enabled intraband transitions. Embedding the nanoparticle in an environment with a sufficiently large dielectric constant removes the contribution from interband hot carriers and enhances the one from intraband hot carriers. These insights from our work pave the way towards a mechanistic understanding of hot-carrier devices. For example, they enable experimentalists to design nanoparticles for specific oxidation and reduction reactions in photocatalysis.

II. FORMALISM FOR HOT-CARRIER GENERATION RATES

When the nanoparticle is illuminated by light with frequency ω, the rate of excited hot electrons with energy E per unit volume can be obtained from Fermi's golden rule according to [33,34]

$$N_e(E,\omega) = \frac{2}{V}\sum_{if}\Gamma_{if}(\omega)\delta(E-E_f;\sigma), \tag{1}$$

where i and f denote the initial and final states (with energies E_i and E_f) of the light-induced electronic transition, V is the nanoparticle volume, and the factor of 2 accounts for spin degeneracy. Also, we defined the Gaussian broadened spectral function $\delta(x;\sigma) \equiv (1/\sqrt{2\pi\sigma^2})\exp(-x^2/2\sigma^2)$, which becomes a delta function in the limit of $\sigma \to 0^+$. Here, σ is a broadening parameter reflecting the finite quasiparticle linewidth. Finally, Γ_{if} is given by

$$\Gamma_{if}(\omega) = \frac{2\pi}{\hbar}|\langle f|\hat{\Phi}_{\mathrm{tot}}(\omega)|i\rangle|^2\delta(E_f - E_i - \hbar\omega;\gamma) \times f(E_i)(1-f(E_f)). \tag{2}$$

Here, $f(E)$ denotes the Fermi-Dirac distribution function that we evaluated at room temperature in this work, but calculations for other temperatures and even nonequilibrium distribution functions are straightforward within our formalism. Also, $\hat{\Phi}_{\mathrm{tot}}(\omega)$ is the total potential operator that consists of two contributions: the field arising from the external illumination and the induced field caused by the electronic response of the nanoparticle. Moreover, γ denotes the typical linewidth of electronic transitions. In previous work [33,34] $\delta(E_f - E_i - \hbar\omega;\gamma)$ was often approximated by a Lorentzian function. However, we have found that this choice introduces artificial peaks near the Fermi level as a consequence of the slow decay of the Lorentzians. A similar expression for the rate of photoexcited hot holes can be obtained by swapping the indices of final and initial states in Eq. (1). We note that our formalism does not capture effects related to light scattering by the nanoparticle.

To numerically evaluate the hot-carrier generation rates in nanoparticles, we employ the tight-binding approach to calculate the electronic states and their energies. Specifically, we assume that all nanoparticle wavefunctions can be expressed as linear combinations of the 3*d*, 4*s*, and 4*p* atomic orbitals for Cu, 4*d*, 5*s*, and 5*p* atomic orbitals for Ag, and the 5*d*, 6*s*, and 6*p* atomic orbitals for Au. The tight-binding Hamiltonian is based on an orthogonal two-center parametrization of *ab initio* density-functional theory calculations [42] and the resulting band structures are in good agreement with *ab initio* results using the augmented plane-wave method with the local density approximation [42]. The total potential is evaluated in the

quasistatic approximation using experimentally measured bulk dielectric functions and the resulting matrix elements are calculated following the approach of Pedersen *et al.* [44]; see Sec. V for details.

The evaluation of Eq. (1) via exact diagonalization methods becomes impractical for large nanoparticles. To overcome this challenge, we exploit the observation that the hot-carrier generation rate, Eq. (1), is a spectral quantity similar to the density of states $\rho(E) = \sum_n \delta(E - E_n)$. For such quantities, highly efficient numerical approaches have recently been developed that avoid the need to diagonalize large Hamiltonian matrices [38–41]. To harness these spectral methods, we write the hot-carrier rate as

$$N_e(E,\omega) = \frac{4\pi}{\hbar V}\int_{-\infty}^{\infty} d\mathcal{E}'\delta(E-\mathcal{E}';\sigma) \times \int_{-\infty}^{\infty} d\mathcal{E}\phi(\mathcal{E},\mathcal{E}',\omega)\delta(\mathcal{E}-\mathcal{E}'-\hbar\omega;\gamma) f(\mathcal{E})(1-f(\mathcal{E}')), \quad (3)$$

where $\phi(\mathcal{E},\mathcal{E}',\omega) = \sum_{if} |\langle f|\hat{\Phi}_{\text{tot}}(\omega)|i\rangle|^2 \delta(\mathcal{E}-E_i)\delta(\mathcal{E}'-E_f)$ can be conveniently expressed as the trace of the operator $\delta(\mathcal{E}-\hat{H})\hat{\Phi}_{\text{tot}}(\omega)\delta(\mathcal{E}'-\hat{H})\hat{\Phi}_{\text{tot}}(\omega)$. In order to apply the full machinery of spectral methods, we rescale and shift the energy variables $\mathcal{E}(\mathcal{E}') \mapsto \varepsilon(\varepsilon')$ and the Hamiltonian $\hat{H} \mapsto \hat{h}$ so that the spectral weight is mapped into the interval $[-1:1]$, where first-kind Chebyshev polynomials, $T_n(\varepsilon) = \cos(n \arccos\varepsilon)$ (with n being a non-negative integer), form a complete set of orthogonal functions [45]. The spectral operator $\delta(\varepsilon - \hat{h})$ can now be formally expressed as an infinite series of Chebyshev polynomials according to $\delta(\varepsilon-\hat{h}) = [2/(\pi\sqrt{1-\varepsilon^2})]\sum_{n=0}^{\infty}(1+\delta_{n0})^{-1}T_n(\hat{h})T_n(\varepsilon)$. In practical calculations, this series is truncated after $N-1$ terms, which induces unphysical Gibbs oscillations. These can be removed by multiplying each term in the series with a coefficient of Jackson's kernel given by $J(n,N) = [(N-n)\cos(\pi n/N) + \sin(\pi n/N)\cot(\pi/N)]/N$ [41,46], which effectively replaces each delta function by a Gaussian (note that the width of these Gaussians is much smaller than the physical broadening parameters σ and γ). Inserting these series into $\phi(\epsilon,\epsilon',\omega)$ gives

$$\phi(\varepsilon,\varepsilon',\omega) \approx \frac{1}{E_-^2}\sum_{n=0}^{N-1}\sum_{m=0}^{N-1}\frac{4\mu_{mn}(\omega)T_m(\varepsilon)T_n(\varepsilon')}{\pi^2\sqrt{(1-\varepsilon^2)(1-\varepsilon'^2)}} \times \frac{J(n,N)J(m,N)}{(1+\delta_{n0})(1+\delta_{m0})}, \quad (4)$$

where we have defined $\mu_{mn}(\omega) = \text{Tr}[T_m(\hat{h})\hat{\Phi}_{\text{tot}}(\omega)T_n(\hat{h})\hat{\Phi}_{\text{tot}}(\omega)]$ that can be computed efficiently exploiting the recurrence relation of Chebyshev polynomials and stochastic trace evaluation techniques [41]; see Sec. V for details.

III. HOT-CARRIER GENERATION RATES

We have calculated hot-carrier generation rates for spherical nanoparticles of Ag, Au, and Cu containing up to 1 072 241 atoms [corresponding to diameters up to 32 nm (Ag), 33 nm (Au), and 28 nm (Cu)].

Figure 1(a) shows the evolution of the hot-electron and hot-hole generation rates in Ag nanoparticles as a function of the diameter when the nanoparticle is illuminated at the LSP frequency (3.5 eV in vacuum). For the smallest nanoparticle ($D = 2$ nm), the hot-electron and hot-hole rates exhibit a series of discrete peaks characteristic of a moleculelike behavior. At a diameter of 4 nm, we find that the hot-electron and hot-hole rates have evolved into smooth curves. The hot-hole rate has a sharp peak near

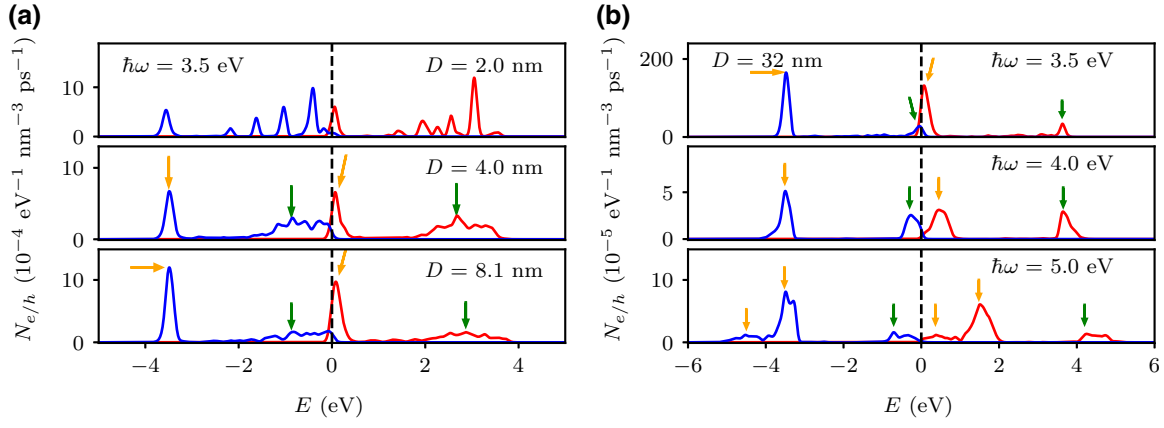

FIG. 1. Hot-carrier generation rates for spherical silver nanoparticles. (a) Dependence of the hot-hole (blue) and hot-electron (red) rates on the nanoparticle diameter D at the LSP frequency. (b) Dependence of hot-carrier rates on the illumination frequency for a $D = 32$ nm nanoparticle. Yellow arrows indicate peaks arising from d-to-sp band transitions and green arrows indicate peaks arising from sp-to-sp band transitions. The zero of energy is set to the Fermi level.

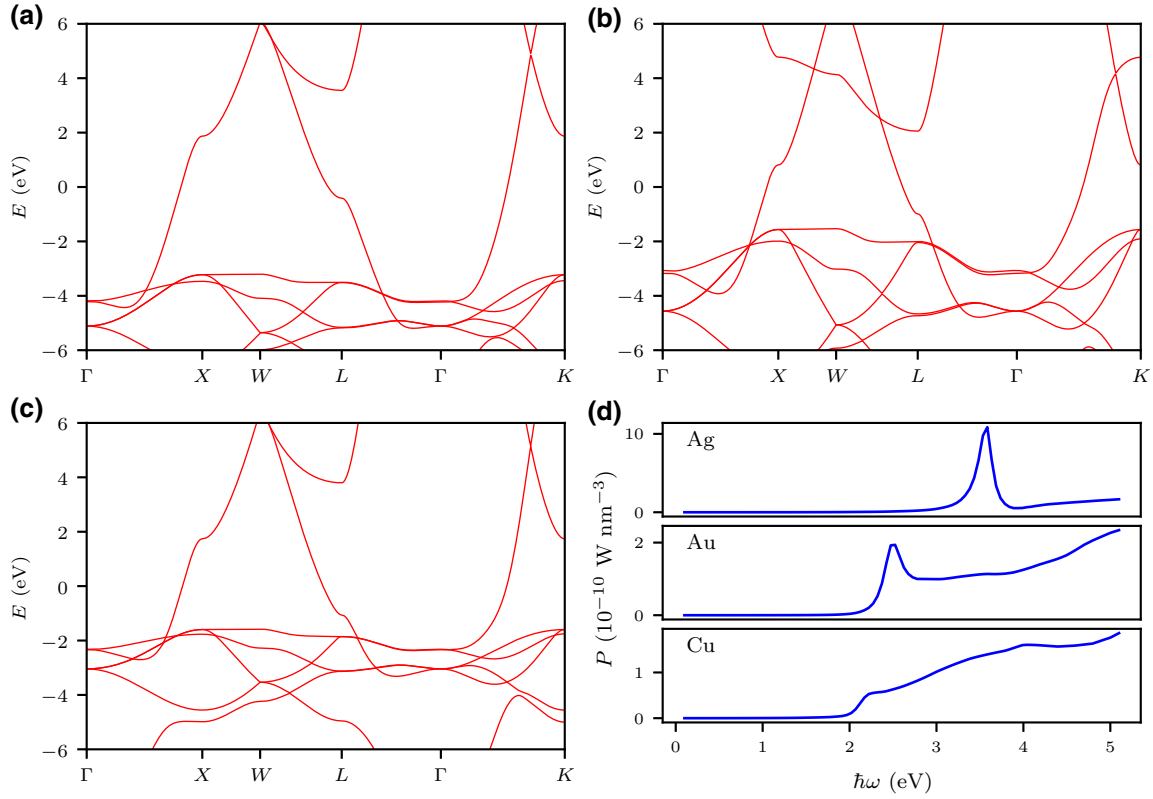

FIG. 2. Electronic band structures of (a) silver, (b) gold, and (c) copper. The zero of energy is set to the Fermi level. (d) The power (for an illumination intensity of 1 mW μm^{-2}) absorbed by the spherical nanoparticles as a function of photon energy.

−3.5 eV (indicated by the yellow arrow) and a second broader peak closer to the Fermi level (indicated by the green arrow). Because of energy conservation, the hot-electron rate also exhibits a sharp peak (indicated by the yellow arrow) that is shifted from the sharp peak in the hot-hole rate by the LSP energy and lies close to the Fermi level. The second peak in the hot-electron rate (which corresponds to the broad peak in the hot-hole rate near the Fermi level and is indicated by a green arrow) is centered near 2.9 eV. The energy of the sharp peak (indicated by the yellow arrow) in the hot-hole rate corresponds to the onset of the flat *d* bands in Ag; see Fig. 2. When the nanoparticle is illuminated with light at the LSP frequency, interband transitions from the *d* band to the *sp* band that cross the Fermi level can be induced. The broad peaks in the hot-electron and hot-hole rates (indicated by green arrows), on the other hand, originate from transitions from *sp*-band states into other *sp*-band states. In contrast to the *d*-to-*sp* transitions, such transitions are forbidden in the bulk material and are only enabled by the presence of the surface. As the size of the nanoparticle increases, we expect the contribution of the surface-enabled transitions to decrease in comparison to the bulk transitions. Indeed, it can be seen that the size of the broad peak is significantly reduced for a diameter of 8.1 nm in comparison to the size of the sharp peak.

Next, we study the dependence of the hot-carrier generation rates on the light frequency. Figure 1(b) shows the hot-electron and hot-hole rates of a Ag nanoparticle with a diameter of 32 nm (corresponding to 1 072 241 atoms) at illumination frequencies of 3.5 eV, 4.0 eV, and 5.0 eV. Again, it can be seen that the hot-electron and hot-hole rates exhibit two peaks. The strongest peak is in the hot-hole rate at around −3.5 eV (which is indicated by a yellow arrow and corresponds to the onset of the *d* bands). The corresponding peak in the hot-electron rate is shifted by the illumination frequency, i.e., it moves to higher energies as the illumination frequency is increased. A second smaller peak in the hot-hole rate (indicated by the green arrow) occurs just below the Fermi level where the density of occupied *sp*-band states is highest. This peak moves to lower energies as the illumination frequency is increased. The corresponding peak in the hot-electron rate is located near 4.0 eV and moves to slightly higher energies as the light frequency is increased. These results show that hot holes are predominantly produced in the *d* band (as a result of *d*-to-*sp* transitions), but also near the Fermi level. In contrast, the energy of hot electrons generated by bulk transitions can be controlled through the illumination frequency, while the energy of surface-enabled hot electrons is very high. It can also be seen that the highest number of hot carriers is produced at the LSP frequency

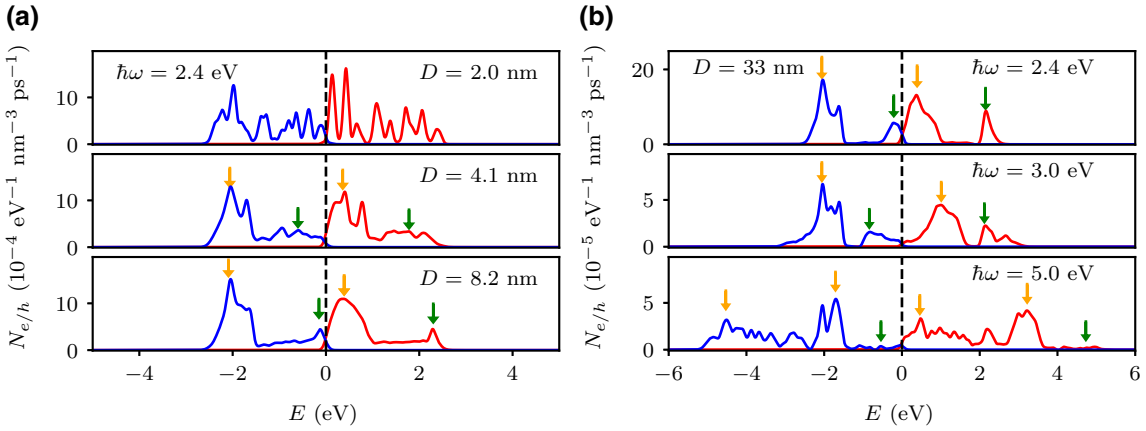

FIG. 3. Hot-carrier generation rates for spherical gold nanoparticles. (a) Dependence of the hot-hole (blue) and hot-electron (rate) rates on the nanoparticle diameter D at the LSP frequency. (b) Dependence of hot-carrier rates on the illumination frequency for the $D = 33$ nm nanoparticle. Yellow arrows indicate peaks arising from d-to-sp band transitions and green arrows indicate peaks arising from sp-to-sp band transitions. The zero of energy is set to the Fermi level.

as a consequence of the large enhancement of the field intensity. At the LSP frequency, bulk transitions are much more frequent than surface-enabled transitions. In contrast, the relative contribution of surface-enabled hot carriers increases for higher illumination frequencies.

Figure 3 shows the hot-carrier rates for Au nanoparticles. At the LSP frequency (2.4 eV in vacuum), the hot-carrier rates again exhibit discrete peaks for small nanoparticles, which evolve into continuous distributions as the diameter increases; see Fig. 3(a). The main peak in the hot-hole rate (indicated by the yellow arrow) for the larger nanoparticles is located at -2.0 eV, corresponding to the onset of d bands in the material; see Fig. 2(b). A corresponding peak in the hot-electron rate is located just above the Fermi level (also indicated by a yellow arrow). Both rates also exhibit a second smaller peak (indicated by green arrows) caused by surface-enabled sp-to-sp transitions. This second peak is just below the Fermi level in the hot-hole rate and near +2.3 eV in the hot-electron rate.

Considering next the evolution as a function of light frequency for a nanoparticle of 33 nm diameter [see Fig. 3(b)] reveals that the main peak (indicated by a yellow arrow) in the hot-hole generation rate remains at -2.0 eV while the corresponding peak in the hot-electron rate moves to higher energies. In contrast to Ag, an additional hot-hole peak emerges at lower energies (near -4.5 eV for a light frequency of 5 eV, also indicated by a yellow arrow) with a corresponding hot-electron peak just above the Fermi level. These peaks result from transitions from deeper

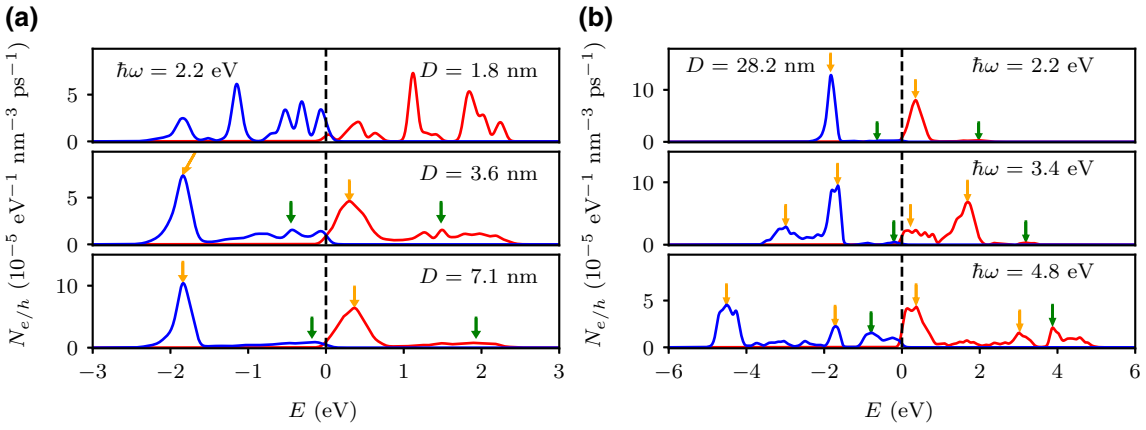

FIG. 4. Hot-carrier generation rates for spherical copper nanoparticles. (a) Dependence of the hot-hole (blue) and hot-electron (rate) rates on the nanoparticle diameter D at the LSP frequency. (b) Dependence of hot-carrier rates on the illumination frequency for the $D = 28.2$ nm nanoparticle. Yellow arrows indicate peaks arising from d-to-sp band transitions and green arrows indicate peaks arising from sp-to-sp band transitions. The zero of energy is set to the Fermi level.

lying *d* bands to *sp* bands. The hot-hole peak just below the Fermi level disappears as the light frequency increases.

After that, we consider Cu nanoparticles. In this system, the LSP peak at 2.2 eV is much less pronounced; see Figs. 2(c) and 2(d). As a consequence, the hot-carrier peaks at the LSP frequency are much lower than in Ag and Au; see Fig. 4(a). Similarly to the case of Ag, we find a peak in the hot-hole rate (indicated by the yellow arrow) at -1.8 eV, corresponding to bulk *d*-to-*sp* transitions with a corresponding hot-electron peak just above the Fermi level. A second smaller peak in the hot hole rate (indicated by the green arrow) arising from the surface-enabled *sp*-to-*sp* transition is found just below the Fermi level and a corresponding hot-electron peak near 2 eV. At higher frequencies, additional peaks at lower energies (indicated by yellow arrows) emerge in the hot-hole rate as a consequence of transitions from low-lying *d* states. In particular, at a light frequency of 4.8 eV the strongest peak is located at -4.5 eV and a corresponding peak in the hot-electron rate is located at $+0.4$ eV.

Finally, we study the dependence of the hot-carrier generation rates on the dielectric constant of the surrounding medium. Figure 5 shows results for a silver nanoparticle with a diameter of 4 nm. As discussed above, in vacuum ($\epsilon_m = 1$), the hot-hole generation rate has a large peak at -3.5 eV due to interband transitions with a corresponding hot-electron peak near the Fermi level (indicated by yellow arrows). For $\epsilon_m = 4$, the LSP frequency has reduced to 3.15 eV. This is no longer sufficient to excite interband transitions and the hot-hole rate is characterized by a broad peak near the Fermi level, while the hot-hole rate exhibits a corresponding peak near 3 eV (indicated by green arrows). Interestingly, the height of the intraband peak is increased compared to the case of vacuum. This increase is caused by an increase in the matrix elements [43,47] that are proportional to $1/\omega^2$ [43]. As the medium dielectric constant increases, the main peak of the hot-hole generation rate remains close to the Fermi level, while the energy of the hot electrons is reduced. These findings demonstrate that hot-carrier generation rates can be controlled by a careful choice of the dielectric properties of the nanoparticle environment.

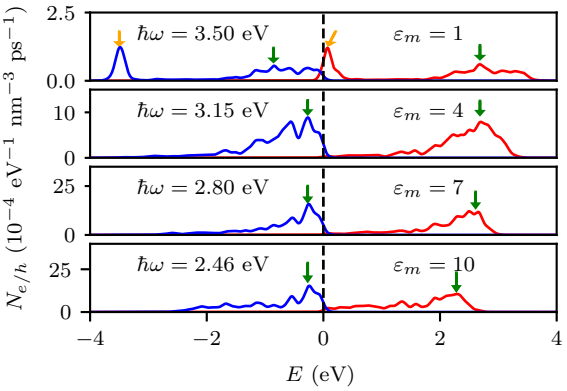

FIG. 5. Hot-carrier distribution of a spherical silver nanoparticle with a diameter of 4 nm in various dielectric environments evaluated at the corresponding LSP frequencies. Yellow arrows indicate peaks arising from *d*-to-*sp* band transitions and green arrows indicate peaks arising from *sp*-to-*sp* band transitions.

IV. CONCLUSION

We have reported atomistic quantum-mechanical calculations of plasmon-induced hot-carrier generation rates in large nanoparticles containing more than one million atoms. Accessing this size regime that is relevant for practical devices is possible through the use of highly efficient spectral methods based on an expansion of the hot-carrier generation rate in terms of Chebyshev polynomials. These advances allow us to study the evolution of the hot-carrier generation rate as a function of nanoparticle diameter from a moleculelike regime characterized by discrete peaks to a continuous curve for diameters exceeding 4 nm. Moreover, the relative importance of bulk *d* band to *sp*-band transitions compared to surface-enabled *sp*-band to *sp*-band transitions increases with increasing diameter. Interband transitions give rise to a large peak in the hot-hole generation rate located at the onset of *d*-band states. Such holes have energies of several electron volts relative to the Fermi level. The corresponding peak in the hot-electron rate lies closer to the Fermi level, but is tunable through the illumination frequency. In contrast, intraband transitions induce holes near the Fermi level and hot electrons with energies of several electron volts. Finally, the contribution to the hot-carrier distributions arising from interband transitions can be removed by increasing the dielectric constant of the surrounding medium that also enhances the matrix elements for intraband transitions. These insights are crucial for fabricating nanoparticles for inducing and optimizing specific chemical reactions. They also form the starting point for studying the thermalization of hot electrons, which is the subject of future work.

V. METHODS

A. Atomic structure of nanoparticles

Spherical nanoparticles of different sizes are carved from the bulk material. Specifically, we first choose an atom as the centre of the nanoparticle and remove all atoms whose distance from the central atom is greater than the nanoparticle radius.

B. Quasistatic approximation

We use the quasistatic approximation to evaluate the total electric potential experienced by electrons in the nanoparticle. If the electric field is parallel to the *z* axis,

the total potential inside the nanoparticle is given by

$$\Phi_{\rm tot}(z,\omega) = -eE_0\frac{3\epsilon_m}{\epsilon(\omega)+2\epsilon_m}z, \quad (5)$$

where E_0 is the electric field strength of the external illumination, ϵ_m denotes the dielectric constant of the medium in which the nanoparticle is embedded, and $\epsilon(\omega)$ denotes the bulk dielectric function of the material [3,33,48]. Here, we use experimental bulk dielectric functions [49] to evaluate $\Phi_{\rm tot}(z,\omega)$. In our calculations, we use $E_0 = 8.7\times 10^5$ V/m, corresponding to an illumination intensity of 1 mW/μm^2. We note that the quasistatic approximation is only accurate for nanoparticles with sizes that are much smaller than the wavelength of light. On the other hand, the use of a bulk dielectric function becomes unreliable for very small nanoparticles where quantum size effects become important.

C. Matrix elements

To calculate the hot-carrier rates, we need to evaluate the matrix element of $\Phi_{\rm tot}(z,\omega)$ between two nanoparticle states. Within the tight-binding method, these states are expressed as linear combinations of atomic orbitals $|i,\alpha\rangle$, where the index i labels the atom of the nanoparticle and the index α labels the orbitals on the atom. Following Pederson and workers [44], the matrix element of the total potential between two atomic orbitals is evaluated as

$$\langle j,\beta|\hat{\Phi}_{\rm tot}(\omega)|i,\alpha\rangle = -eE_0\frac{3\epsilon_m}{\epsilon(\omega)+2\epsilon_m}(z_j + d_{\alpha,\beta})\delta_{ij}, \quad (6)$$

where z_j denotes the z coordinate of atom j and $d_{\alpha,\beta}$ is the intra-atomic dipole matrix element between orbitals $|\alpha\rangle$ and $|\beta\rangle$. We calculate the intra-atomic matrix element using *ab initio* density-functional theory for isolated atoms as implemented in the electronic structure program FHI-aims [50]. In these calculations, the Perdew-Burke-Ernzerhof exchange-correlation functional [51] is used. Non-spin-polarized calculations are performed in all cases, resulting in an $(n-1)d^{10}ns^1$ valence electron configuration for Cu, Ag, and Au. Scalar relativistic effects are included via the atomic ZORA formalism, and the FHI-aims default "tight" numerical basis sets are employed [50,52]. In order to ensure that the calculated Kohn-Sham orbitals and the corresponding matrix elements match the canonical atomic orbital basis functions used in the tight-binding calculations, a small external potential that lifts the degeneracies of the metal d and p orbitals is introduced in the DFT calculations. It is verified that the external potential does not affect the energies of the Kohn-Sham eigenstates by more than 0.01 eV. The nonvanishing matrix elements are shown in Table I.

TABLE I. Nonvanishing intra-atomic dipole matrix elements obtained from first-principles calculations; see the text.

		$d_{\alpha,\beta}$ (10^{-2} nm)		
α	β	Ag	Au	Cu
d_{zx}	p_x	2.73	3.27	2.31
d_{yz}	p_z	2.73	3.27	2.31
d_{z^2}	p_z	3.15	3.75	2.63
s	p_z	9.36	8.95	8.55

D. Spectral approach

To expand the spectral operator $\delta(E-\hat{H})$ in terms of Chebyshev polynomials, the energy variable and the Hamiltonian must be rescaled and shifted such that their spectral weight lies in the interval $[-1;1]$. This is achieved by the following transformation: $\varepsilon = (\mathcal{E}-E_+)/E_-$ and $\hat{h} = (\hat{H}-E_+)/E_-$ with $E_\pm = (E_L \pm E_S)/2$ and $E_{L(S)}$ the largest (smallest) energy level of the nanoparticle, which is approximated by the largest (smallest) energy of the bulk band structure. Truncating the series expansion of the spectral operator and multiplying each term with the coefficients of Jackson's kernel, effectively replaces the delta function by a Gaussian with an energy-dependent width. The chosen value of $N = 5000$ gives rise to a maximum broadening of 12 meV for Ag, 9.5 meV for Au, and 12 meV for Cu. These numerical broadenings are significantly smaller than the physical broadening parameters ($\sigma = 50$ meV and $\gamma = 60$ meV) that we use in our calculations.

Finally, evaluating $\phi(\epsilon,\epsilon',\omega)$ requires computation of the Chebyshev moments defined as $\mu_{mn}(\omega) = {\rm Tr}[T_m(\hat{h})\hat{\Phi}_{\rm tot}(\omega)T_n(\hat{h})\hat{\Phi}_{\rm tot}(\omega)]$. This is achieved by using the recurrence relation of the Chebyshev polynomials and a stochastic trace evaluation technique that scales linearly with system size. In particular, we approximate

$$\mu_{mn}(\omega) \approx \left|eE_0\frac{3\epsilon_m}{\epsilon(\omega)+2\epsilon_m}\right|^2 \sum_{k=1}^{K}\langle k|T_m(\hat{h})\hat{z}T_n(\hat{h})\hat{z}|k\rangle, \quad (7)$$

where $\{|k\rangle\}$ denotes a set of random vectors. As the system size increases, the number K of vectors in this set required for converged results decreases. In our calculations, we have used 100–10 000 random vectors depending on the diameter of the nanoparticle that results in highly converged results.

ACKNOWLEDGMENTS

J.L. and A.F. acknowledge funding from the Royal Society through a Royal Society University Research Fellowship. This project has received funding from the European Union's Horizon 2020 research and innovation

programme under Grant Agreement No. 892943. J.M.K. acknowledges support from the Estonian Centre of Excellence in Research project "Advanced materials and high-technology devices for sustainable energetics, sensorics and nanoelectronics" TK141 (2014-2020.4.01.15-0011).

[1] C. Clavero, Plasmon-induced hot-electron generation at nanoparticle/metal-oxide interfaces for photovoltaic and photocatalytic devices, Nat. Photonics **8**, 95 (2014).
[2] U. Aslam, V. G. Rao, S. Chavez, and S. Linic, Catalytic conversion of solar to chemical energy on plasmonic metal nanostructures, Nat. Catalysis **1**, 656 (2018).
[3] S. Maier, *Plasmonics* (Springer, Boston, 2007).
[4] A. M. Brown, R. Sundararaman, P. Narang, W. A. Goddard, and H. A. Atwater, Nonradiative plasmon decay and hot carrier dynamics: Effects of phonons, surfaces, and geometry, ACS Nano **10**, 957 (2015).
[5] S. Link and M. A. El-Sayed, Spectral properties and relaxation dynamics of surface plasmon electronic oscillations in gold and silver nanodots and nanorods, J. Phys. Chem. B **103**, 8410 (1999).
[6] M. L. Brongersma, N. J. Halas, and P. Nordlander, Plasmon-induced hot carrier science and technology, Nat. Nanotechnol. **10**, 25 (2015).
[7] A. O. Govorov, W. Zhang, T. Skeini, H. Richardson, J. Lee, and N. A. Kotov, Gold nanoparticle ensembles as heaters and actuators: Melting and collective plasmon resonances, Nanoscale Res. Lett. **1**, 84 (2006).
[8] G. V. Hartland, L. V. Besteiro, P. Johns, and A. O. Govorov, What's so hot about electrons in metal nanoparticles?, ACS Energy Lett. **2**, 1641 (2017).
[9] A. FujiShima and K. Honda, Electrochemical photolysis of water at a semiconductor electrode, Nature **238**, 37 (1972).
[10] F. Enrichi, A. Quandt, and G. Righini, Plasmonic enhanced solar cells: summary of possible strategies and recent results, Renewable Sustainable Energy Rev. **82**, 2433 (2018).
[11] M. L. Salvador, B. A. MacLeod, A. Hess, A. P. Kulkarni, K. Munechika, J. I. L. Chen, and D. S. Ginger, Electron accumulation on metal nanoparticles in plasmon-enhanced organic solar cells, ACS Nano **6**, 10024 (2012).
[12] L. Yan, F. Wang, and S. Meng, Quantum mode selectivity of plasmon-induced water splitting on gold nanoparticles, ACS Nano **10**, 5452 (2016).
[13] I. Thomann, B. Pinaud, Z. Chen, B. A. Clemens, T. F. Jaramillo, and M. L. Brongersma, Plasmon enhanced solar-to-fuel energy conversion, Nano Lett. **11**, 3440 (2011).
[14] I. Goykhman, B. Desiatov, J. Khurgin, J. Shappir, and U. Levy, Locally oxidized silicon surface-plasmon Schottky detector for telecom regime, Nano Lett. **11**, 2219 (2011).
[15] W. Li and J. G. Valentine, Harvesting the loss: surface plasmon-based hot electron photodetection, Nanophotonics **6**, 177 (2017).
[16] H. Chalabi, D. Schoen, and M. L. Brongersma, Hot-electron photodetection with a plasmonic nanostripe antenna, Nano Lett. **14**, 1374 (2014).
[17] H. Tang, C. Chen, Z. Huang, J. Bright, G. Meng, R. Liu, and N. Wu, Plasmonic hot electrons for sensing, photodetection, and solar energy applications: A perspective, J. Chem. Phys. **152**, 220901 (2020).
[18] Q. Sun, C. Zhang, W. Shao, and X. Li, Photodetection by hot electrons or hot holes: A comparable study on physics and performances, ACS Omega **4**, 6020 (2019).
[19] Y. Zhai, G. Chen, J. Ji, X. Ma, Z. Wu, Y. Li, and Q. Wang, Large-scale, broadband absorber based on three-dimensional aluminum nanospike arrays substrate for surface plasmon induced hot electrons photodetection, Nanotechnology **30**, 375201 (2019).
[20] Y. Zhu, H. Xu, P. Yu, and Z. Wang, Engineering plasmonic hot carrier dynamics toward efficient photodetection, Appl. Phys. Rev. **8**, 021305 (2021).
[21] Y. Dubi, I. W. Un, and Y. Sivan, Thermal effects—an alternative mechanism for plasmon-assisted photocatalysis, Chem. Sci. **11**, 5017 (2020).
[22] Y. Sivan, J. Baraban, I. Un, and Y. Dubi, Comment On "Quantifying hot carrier and thermal contributions in plasmonic photocatalysis", Science **364**, 6439 (2019).
[23] J. B. Khurgin, Hot carriers generated by plasmons: where are they generated and where do they go from there?, Faraday Discuss. **214**, 35 (2019).
[24] J. S. DuChene, G. Tagliabue, A. J. Welch, W. Cheng, and H. A. Atwater, Hot hole collection and photoelectrochemical CO_2 reduction with plasmonic Au/p-GaN photocathodes, Nano Lett. **18**, 2545 (2018).
[25] G. Baffou, F. Cichos, and R. Quidant, Applications and challenges of thermoplasmonics, Nat. Mater. **19**, 946 (2020).
[26] R. Sundararaman, P. Narang, A. S. Jermyn, W. A. Goddard III, and H. A. Atwater, Theoretical predictions for hot-carrier generation from surface plasmon decay, Nat. Commun. **5**, 5788 (2014).
[27] M. Bernardi, J. Mustafa, J. B. Neaton, and S. G. Louie, Theory and computation of hot carriers generated by surface plasmon polaritons in noble metals, Nat. Commun. **6**, 7044 (2015).
[28] A. M. Brown, R. Sundararaman, P. Narang, W. A. Goddard, and H. A. Atwater, Ab initiophonon coupling and optical response of hot electrons in plasmonic metals, Phys. Rev. B **94**, 075120 (2016).
[29] J. Zhang, M. Guan, J. Lischner, S. Meng, and O. V. Prezhdo, Coexistence of different charge-transfer mechanisms in the hot-carrier dynamics of hybrid plasmonic nanomaterials, Nano Lett. **19**, 3187 (2019).
[30] L. R. Castellanos, O. Hess, and J. Lischner, Single plasmon hot carrier generation in metallic nanoparticles, Commun. Phys. **2**, 47 (2019).
[31] T. P. Rossi, P. Erhart, and M. Kuisma, Hot-carrier generation in plasmonic nanoparticles: the importance of atomic structure, ACS Nano **14**, 9963 (2020).
[32] E. Prodan and P. Nordlander, Electronic structure and polarizability of metallic nanoshells, Chem. Phys. Lett. **352**, 140 (2002).
[33] A. Manjavacas, J. G. Liu, V. Kulkarni, and P. Nordlander, Plasmon-induced hot carriers in metallic nanoparticles, ACS Nano **8**, 7630 (2014).

[34] S. D. Forno, L. Ranno, and L. Lischner, Material, size, and environment dependence of plasmon-induced hot carriers in metallic nanoparticles, J. Phys. Chem. **122**, 8517 (2018).
[35] L. Ranno, S. D. Forno, and J. Lischner, Computational design of bimetallic core-shell nanoparticles for hot-carrier photocatalysis, npj Comput. Mater. **4**, 31 (2018).
[36] A. J. Wilson, V. Mohan, and P. K. Jain, Mechanistic understanding of plasmon-enhanced electrochemistry, J. Phys. Chem. **123**, 29360 (2019).
[37] G. Tagliabue, H. A. Atwater, *et al.*, Ultrafast hot-hole injection modifies hot-electron dynamics in Au/p-GaN heterostructures, Nat. Mater. **19**, 1312 (2020).
[38] S. M. João, M. Andelković, L. Covaci, T. G. Rappoport, J. M. V. P. Lopes, and A. Ferreira, KITE: high-performance accurate modelling of electronic structure and response functions of large molecules, disordered crystals and heterostructures, R. Soc. Open Sci. **7**, 191809 (2020).
[39] S. M. João and J. M. V. P. Lopes, Basis-independent spectral methods for non-linear optical response in arbitrary tight-binding models, J. Condens. Matter Phys. **32**, 125901 (2019).
[40] A. Ferreira and E. Mucciolo, Critical Delocalization Of Chiral Zero Energy Modes in Graphene, Phys. Rev. Lett. **115**, 106601 (2015).
[41] A. Weiße, G. Wellein, A. Alvermann, and H. Fehske, The Kernel polynomial method, Rev. Mod. Phys. **78**, 275 (2006).
[42] D. Papaconstantopoulos, *Handbook of the Band Structure of Elemental Solids* (Springer, New York, 2015).
[43] L. R. Castellanos, J. Kahk, O. Hess, and J. Lischner, Generation of plasmonic hot carriers from D-bands in metallic nanoparticles, J. Chem. Phys. **152**, 104111 (2020).
[44] T. Pedersen, K. Pedersen, and T. B. Kriestensen, Optical matrix elements in tight-binding calculations, Phys. Rev. B **63**, 201101 (2001).
[45] J. P. Boyd, *Chebyshev & Fourier Spectral Methods* (Dover, New York, 2001).
[46] D. Jackson, *Über die Genauigkeit der Annäherung Stetiger Funktionen Durch Ganze Rationale Funktionen Gegebenen Grades und Trigonometrische Summen Gegebener Ordnung* (Dieterich, Göttingen, 1911).
[47] L. R. Castellanos, O. Hess, and J. Lischner, Dielectric engineering of hot-carrier generation by quantized plasmons in embedded silver nanoparticles, J. Phys. Chem. **125**, 3081 (2021).
[48] J. Otsuki, K. Sugawa, and S. Jin, Plasmonic triangular nanoprism sensors, Adv. Mater. **2**, 32 (2021).
[49] H. William, *CRC Handbook of Chemistry and Physics: A Ready-Reference Book of Chemical and Physical Data* (CRC Press, Boca Raton, FL, 2015).
[50] V. Blum, R. Gehrke, F. Hanke, P. Havu, V. Havu, X. Ren, K. Reuter, and M. Scheffler, Ab initio molecular simulations with numeric atom-centered orbitals, Comput. Phys. Commun. **180**, 2175 (2009).
[51] J. P. Perdew, K. Burke, and M. Ernzerhof, Generalized Gradient Approximation Made Simple, Phys. Rev. Lett. **77**, 3865 (1996).
[52] E. V. Lenthe, E. J. Baerends, and J. G. Snijders, Relativistic total energy using regular approximations, J. Chem. Phys. **101**, 9783 (1994).